Estimating Seismic Intensity Maps of the 2021 *M*w 7.3 Madoi, Qinghai and *M*w 6.1 Yangbi, Yunnan, China Earthquakes

Wenkai Chen[1], Dun Wang[*2], Can Zhang[1], Qiang Yao[2], Hongjun Si[3]

1. *Lanzhou Institute of Seismology, China Earthquake Administration, Lanzhou* 730000, *China*
2. *State Key Laboratory of Geological Processes and Mineral Resources, School of Earth Sciences, China University of Geosciences, Wuhan* 430074, *China*
3. *Seismological Research Institute Inc., Tokyo* 113-0032, *Japan*

Wenkai Chen: https://orcid.org/0000-0003-3235-5861; Dun Wang: https://orcid.org/0000-0001-6435-9168

ABSTRACT: This study focuses on rapidly determining seismic intensity maps of earthquakes because it offers fundamental information for effective emergency rescue and subsequent scientific research, and remains challenging to accurately determine seismic intensity map in regions with sparse instrumental observations. Here we applied a novel method that consisted of array technology (back-projection), ground-motion prediction equations, and site corrections, to estimate the seismic intensity maps of the 2021 *M*w 7.3 Madoi, Qinghai and the *M*w 6.1 Yangbi, Yunnan, China earthquakes. We used seismic data recorded at European stations to back-project the source processes of the 2021 *M*w 7.3 Madoi, Qinghai and the *M*w 6.1 Yangbi, Yunnan, China earthquakes. The back-projected energy radiations were then used as subevents or used to define the fault geometry. Summing the contributions of each subevent or estimating the shortest distances from each site to the rupture fault, we obtained the ground motion (PGA and PGV) for each site under rock site conditions. The estimated ground motions were corrected at each site for local site amplification according to the Vs30 database. Our estimated seismic intensity maps and field reports showed high similarity, which further validated the effectiveness of the novel approach, and pushed the limit of earthquake size down to ~*M* 6. Such efforts would substantially help in the fast and accurate evaluation of earthquake damage, and precise rescue efforts.
KEY WORDS: earthquakes, seismic intensity map, back-projection, ground-motion prediction equations.

0   INTRODUCTION

Immediately after large earthquakes, the most important concern is to evaluate the intensity and area of earthquake damage (Cui et al., 2021; Lee and Kiremidjian, 2007; Musson, 2005), because it offers fundamental information for scientific and effective emergency rescue (Wang et al., 2013). Many methods have been developed for the rapid determination of seismic intensity maps after earthquakes (Smith and Mooney, 2021; Farhadi and Pezeshk, 2020; Dong and Shan, 2013; Pathier et al., 2006). In areas with dense real-time strong motion stations, shaking maps can be produced by contouring shaking information interpolated onto the target area (Wald et al., 1999). However, such dense observations are only available in a few countries and areas, such as southern California and Japan. Most regions lack or had sparse real-time strong motion observations. For those regions, the predicted ground motions are mainly calculated based on the earthquake location, the earthquake magnitude, and ground-motion prediction equations (GMPEs).

Individuals using their smartphones have directly reported the intensity of ground motions in earthquake affected regions. With the spread of smartphones and convenient Internet access, individual feeling reports can be rapidly collected and processed to complement or even generate seismic intensity maps (e.g., the DYFI (Did You Feel It?) program at the USGS, Beroza, 2013; Wald et al., 2012; Atkinson and Wald, 2007).

Geodetic observations play an important role in estimating the field damage caused by large earthquakes. At present, there are many types of remote sensing data that can be used, such as optical images, LiDAR, and SAR images (Sharma et al., 2017; Dong and Shan, 2013; Matsuoka and Yamazaki, 2004; Suga et al., 2001; Gamba and Casciati, 1998). Remote sensing images can visually map the earthquake-affected areas and identify the degree of earthquake damage (He et al., 2021; Wang et al., 2015). In addition, the degree of building damage and secondary geological hazards such as barrier lakes can be identified through post-earthquake SAR images (Fan et al., 2012; Gong et al., 2010). Compared to the above-mentioned methods, the acquisition of remote sensing data usually takes days, which limits its practical application in earthquake emergency response.

Among the above methods, the strong motion monitoring method has the best time efficiency, fastest, and most accurate response. However, dense observations are not available every-

where in the world. Sparse real-time strong motion observations are common for most regions, especially in developing and undeveloped countries.

We have proposed a novel algorithm to estimate seismic intensity maps of earthquakes using array technology, GMPEs, and site corrections (Chen et al., 2022). The algorithm was applied to and verified by the 2008 Mw 7.9 Wenchuan and the 2010 Mw 6.9 Yushu earthquakes. Following this method, a preliminary seismic intensity map of the 2021 Mw 7.3 Madoi Earthquake was produced and issued approximately ~4 h after the earthquake, and showed high similarity with the investigated seismic intensity distributions conducted by the China Earthquake Administration (CEA).

To further investigate the effectiveness and applicability of the algorithm we examine the Mw 6.1 Yangbi Earthquake in Yunnan and Mw 7.3 Madoi Earthquake in Qinghai, and evaluated the applicability and accuracy of the algorithm.

1   METHODOLOGY

To rapidly estimate the shaking intensity following damaging earthquakes, we have proposed a novel approach using a combination of array technology, multi-source GMPEs, and site corrections (Chen et al., 2022). By incorporating array technology, we can consider the effects of fault geometries, which significantly improves the accuracy of the estimated seismic intensity map. The method uses three steps: estimation of source energy radiation, calculations of PGA and PGV according to GMPEs, and site corrections.

We first performed a back-projection analysis to acquire the seismic source energy radiation, following the method of Krüger and Ohrnberger (2005), with details in Wang et al. (2016). We presumed that the grid point location with the maximum stacked value at each time window was a subevent of the target earthquake, and its stacked value was thus proportional to the seismic moment or high-frequency seismic energy radiation of the subevent. The rupture front likely radiates more high-frequency energy because of the brittle failure, we filtered broadband seismograms into high-frequency bands prior to the linear stacks in back-projections.

We then calculated the seismic intensity using three models as follows: (1) We assumed that the relative amplitudes and locations of the subevents represent those of the earthquake seismic moment releases. Based on the locations and normalized amplitude of the subevents, we utilized the GMPEs of Si and Midorikawa (1999) employing the equivalent hypocentral distance (EHD) (see Ohno et al., 1993) to calculate the PGAs and PGVs. (2) Similar to Model 1, all the subevents were set to have equal seismic moment releases, and only the spatial locations of subevents derived from back-projections were considered when calculating the ground motions. (3) This model used the GMPEs of Si and Midorikawa (1999), who employed the closest distance from a seismic fault to the calculation point, and only the imaged fault(s) geometry was utilized to calculate the ground motion.

The PGVs on the ground surface were estimated based on the PGVs on stiff ground with Vs30 = 600 m/s predicted by Si and Midorikawa (1999), and information about the average shear-wave velocity in the upper 30 m of sediments (Vs30)

(Thompson et al., 2014; Liu et al., 2013; Boore, 2005; Midorikawa, 1994; Fukushima and Tanaka, 1990).

Following the above three steps, the PGA and PGV for each site were estimated using the back-projected source information, GMPEs, and site conditions (Vs30). We converted the site corrected PGVs to the China seismic intensity scale (GB/T 17742-2020) to compare our estimates with field investigations by the CEA for the 2021 Mw 6.1 Yangbi and Mw 7.3 Madoi, China earthquakes.

2 Mw 6.1 YANGBI, YUNNAN AND Mw 7.3 MADOI, QINGHAI, CHINA EARTHQUAKES

In recent years, many earthquake disasters have occurred in China, causing a large number of casualties and heavy economic losses, such as the 2008 Mw 7.9 Wenchuan Earthquake in Sichuan, the 2010 Mw 6.9 Yushu Earthquake in Qinghai, the 2014 Mw 6.2 Ludian Earthquake in Yunnan, and the 2013 Mw 6.6 Lushan Earthquake in Sichuan. Two recent examples are the 2021 Mw 6.1 Yangbi Earthquake in Yunnan and the Mw 7.3 Madoi Earthquake in Qinghai (Fig. 1).

At 21:48 on May 21, 2021 (Beijing Time), a strong earthquake of Mw 6.1 (25.67°N, 99.87°E, depth 8 km) occurred in Yangbi, Dali Bai Autonomous Prefecture, Yunnan Province, China, which caused severe damages in six counties (cities), including Yangbi, Dali, Eryuan, Weishan, Yunlong, and Yongping counties to varying degrees. Three people died, and 34 were injured (Yunnan Province Seismological Bureau, 2021). The seismogenic fault was believed to be the Weixi-Qiaohou fault; however, no obvious pre-existing surface rupture was observed. The aftershock distribution indicated that the seismogenic fault might be a sub-branch of the Weixi-Qiaohou fault, which had not been previously mapped (Yang et al., 2021; Zhang K L et al., 2021).

Approximately 4 h after the Mw 6.1 Yangbi Earthquake, an earthquake with a Mw of 7.3 (34.5ºN, 98.34ºE, depth 17 km) occurred in Madoi, Qinghai Province at 2:04 on May 22, 2021. Fortunately, the source region was in a rural area with a sparse population, and no casualties were reported. The earthquake occurred in the BayanHar Block, which is one of the main active blocks of the Tibetan Plateau and is bounded by some large-scale active faults, such as the Kunlun fault zone, Xianshuihe-Xiaojiang fault zone, and Longmen Shan thrust belt (Ren and Zhang, 2019; Zhang et al., 2003). Many strong earthquakes have occurred around the BayanHar Block since the 1997 Manyi Earthquake (Ren and Zhang, 2019) and the Madoi Earthquake is the most recent earthquake along the Kunlun fault zone. The seismogenic fault of the Madoi Earthquake belongs to the Kunlun Mountain-Jiangcuo fault system (Ha et al., 2021; Pan et al., 2021; Wang et al., 2021; Zhang C et al., 2021). The Kunlun Mountain-Jiangcuo fault trace extends for approximately 650 km, westward toward the Kunlun fault, which was partially ruptured during the 2001 Kunlun Mw 7.8 Earthquake. The ruptured fault of the Madoi Earthquake is a sub-branch of the Kunlun fault zone, characterized by a left-lateral strike-slip. The co-seismic surface rupture zone of the Madoi Earthquake is approximately 150 km in length, which is consistent with the aftershock distribution shown in Fig. 1 (Pan et al., 2021; Wang et al., 2021).
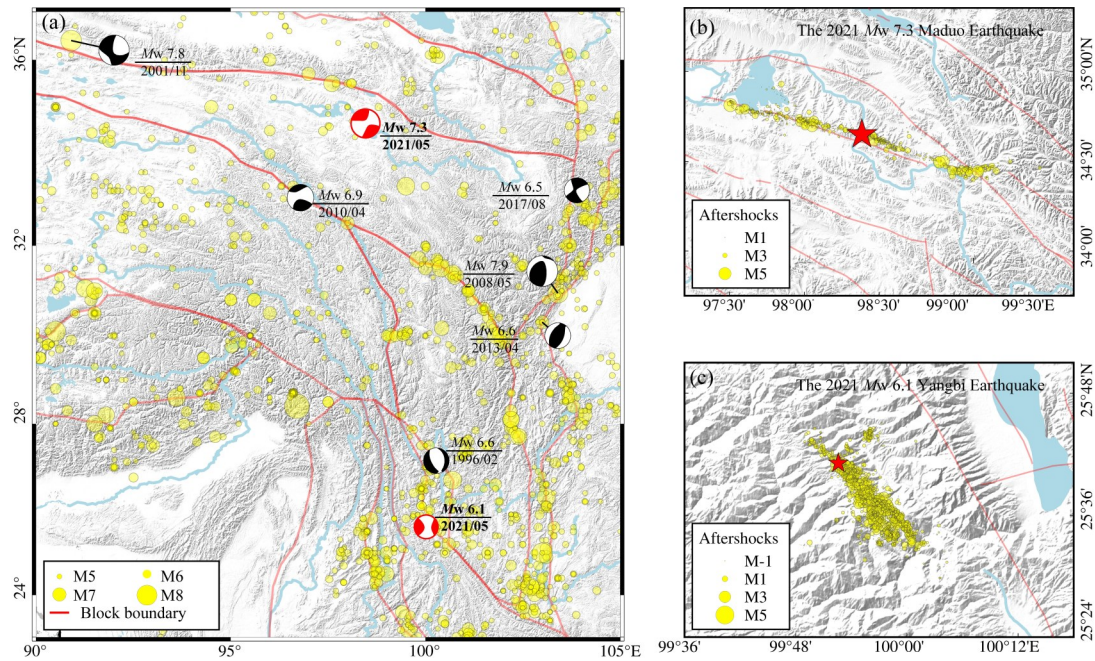
Figure 1. (a) Seismicity and surface faults in the source region. The yellow circles indicate the locations of $M \geqslant 5$ earthquakes (since 1990) from the CEA. The focal mechanisms are from the Global CMT Program. The red lines represent the main block boundaries. (b) Locations of the 2021 *M*w 7.3 Madoi Earthquake sequence. The red star and yellow circles show the epicenter and aftershocks, respectively. (c) The same as (b) plotted for the 2021 *M*w 6.1 Yangbi Earthquake.
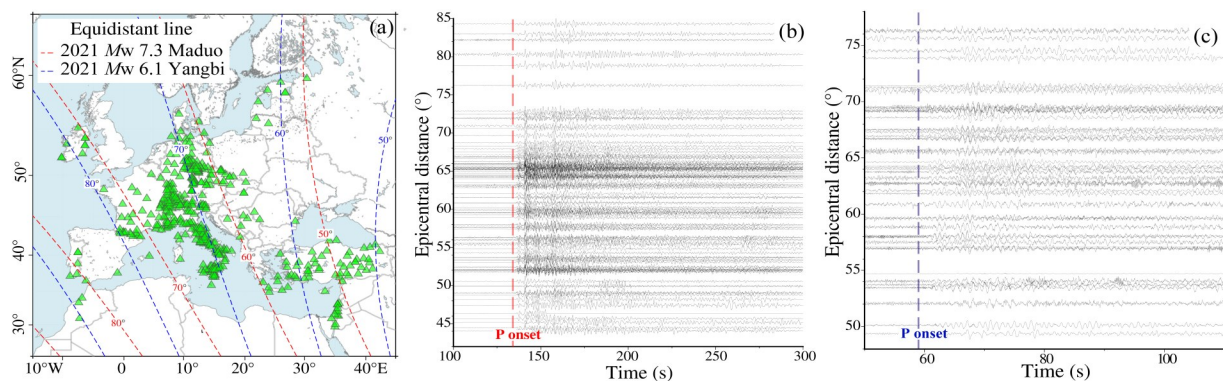

Figure 2. (a) Locations of seismic stations (green triangles). The red dashed lines represent the equidistant lines of the 2021 *M*w 7.3 Madoi Earthquake, and the blue dashed lines represent the equidistant lines of the 2021 *M*w 6.1 Yangbi Earthquake. (b) Representative waveforms of the 2021 *M*w 7.3 Madoi, Qinghai Earthquake recorded in the European seismic network. The waveforms are aligned at the P onset, as indicated by the red dashed line. (c) The same as (b) except for the 2021 *M*w 6.1 Yangbi, Yunnan Earthquake.

3   SOURCE PROCESSES OF THE TWO EARTH-QUAKES

We used seismic data recorded at the European virtual broadband Seismic Network to back-project the rupture processes of the Madoi and Yangbi earthquakes. The European seismic network consists of more than 50 network operators and ~500 seismic stations. The epicentral distances range from 44° to 85° with azimuths of 283° to 335° with respect to the Yangbi Earthquake, and from 296° to 330° with azimuths of 47° to 85° for the Madoi Earthquake.

For the Yangbi Earthquake, we set up a grid of 300 × 300 points (the space grid was 1 km, at a depth of 8 km) that covered the areas with strong ground motion. Following CEA, the epicenter was set at E = 99.87° and N = 25.67°. The seismic waveforms were filtered in the band of 0.8 to 8.0 Hz using a

two-pole Butterworth filter. The filtered waveforms showed high similarities (Fig. 2), which was important for back-projections. We eliminated waveforms with heavy noise and/or strong site effects by setting a threshold value of 0.4 for the correlation coefficient of the waveforms. We stacked the 10 s time windows that were offset by 1 s.

Figure 3b shows the size and spatial distribution of the energy release for the Yangbi Earthquake. The earthquake rupture started from the epicenter with a strong energy radiation for the first 5 to 10 s near the epicenter, and then propagated southeast unilaterally for a few minutes. The total duration was 10–15 s, and the surface length was approximately 20 km. The ruptured fault lineation was compatible with distribution pattern of aftershocks one month following the mainshock (Fig. 1).

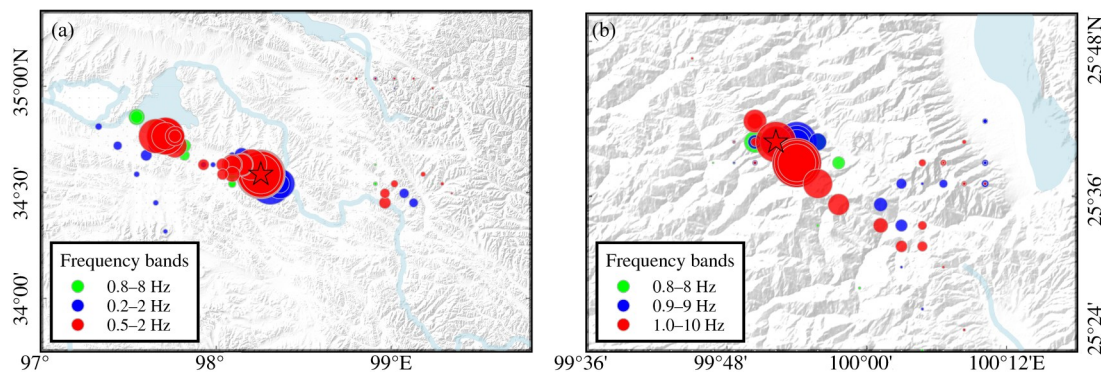For the Madoi Earthquake, we set up a grid of 400 × 400

Figure 3. (a) Locations and amplitudes for the stack, with the maximum amplitude at each time step for the 2021 *M*w 7.3 Madoi Earthquake. The back-projection results are obtained from stacks of the seismograms filtered in three frequency bands (0.2–2.0, 0.5–5.0, and 0.8–8.0 Hz). The lack star represents the epicenter determined by the USGS. (b) The same as (a) except for the 2021 *M*w 6.1 Yangbi Earthquake. The black star represents the epicenter determined by the USGS.

points (spaced at 1 km, at a depth of 17 km) that covered the areas with possible earthquake faults. Following the USGS, the epicenter was set at E = 98.34° and N = 34.50°. The seismic waveforms were filtered in the 0.8 to 8.0 Hz band using a two-pole Butterworth filter. The other parameters were the same as those for the Yangbi case.

Figure 3a shows the size and spatial distribution of the energy release for the Madoi Earthquake. The earthquake rupture started from the epicenter with strong energy radiation in the first 10 s and then propagated bilaterally to the northwest and southeast. The total source duration was ~30 s, and the projected surface length of the rupture was ~150 km. The ruptured fault lineation was compatible with the distribution pattern of aftershocks one month following the mainshock (Fig. 1). The initial rupture speed was relatively slow, and the later part of the rupture speed was ~ 4 km/s, which could be as fast as the local shear wave velocity (super shear). The very fast rupture velocity was previously identified and validated by near-filed and tele-seismic observations (Wang and Mori, 2012; Zhang and Ge, 2010).

4   SEISMIC INTENSITY MAPS

Utilizing the rupture processes of the two earthquakes derived from the back-projections and the above-mentioned GMPEs, we estimated the PGAs and PGVs for each site point. Then the PGVs on the ground surface were estimated based on the PGVs on stiff ground with Vs30 = 600 m/s predicted by Si and Midorikawa (1999).

The site corrected PGVs were then converted to the China seismic intensity scale (GB/T 17742-2020) to compare our estimates with field investigations by the CEA for the 2021 *Mw* 6.1 Yangbi and *Mw* 7.3 Madoi, China earthquakes.

The intensity map of the Yangbi Earthquake (Fig. 4) shows that the severely damaged areas from the three models were all around the epicenter, except that Model 3 showed a southeast extension of the damaged areas. There were also some differences among the amplitudes of the highest intensity. The highest intensity derived from Model 3 was IX, which was 1 degree higher than the investigated intensity map (IIM) and those of derived from models 1 and 2. Careful comparisons indicated that the intensity map produced from Model 1 best matched the IIM. For example, the highest intensity

(VIII), intensities VI and VII areas in Model 1 were very similar to those of the IIM although there are a few isolated intensity VII areas shown in our calculation, which were not observed in the IIM. The isolated intensity VII area was Erhai Lake, which had a very low shear wave velocity at shallow depths and presented amplified ground shakings after site corrections.

Following a similar process, we calculated the intensity maps of the Madoi and Qinghai earthquakes (Fig. 5). Intensity maps derived from the three models shared the common pattern that the highest intensity (IX or above) areas were concentrated in the vicinity and northwest of the epicenter. Since models 2 and 3 highlight more the locations of the subevents derived from the back-projection and ignored the relative amplitudes of the stacked energy, the subevents with relatively small, stacked amplitudes in the west to the epicenter contributed to a large, isolated damage zone with intensity IX (the isolated intensity IX region in the east to the epicenter). Comparisons with IIM indicated that the Model 3 works best in this case, although the area with high intensity (VII–X) in our estimate was somewhat larger than that of the IIM (Fig. 6). However, the contour lines of intensities VII–IX outline the rupture orientation well, which was confirmed by the aftershock locations, field investigation, and geodetic observations (Wang et al., 2021; Ren et al., 2007).

5   DISCUSSION

5.1   Importance of Rapid Damage Estimation in Minutes

Currently, back-projection results can be obtained 10 – 20 min after earthquakes (Song et al., 2019; Yao et al., 2019), the calculations of GMPEs and site corrections for the seismic intensities of grid sites is very fast (within a few minutes), and the seismic intensity map of earthquakes can be produced in less than 30 min. Such information is critical for rapid emergency operations, such as casualty estimation, rescue team deployment, and evacuation of people at risk.

The seismic intensity map, together with back-projected fault traces, represents a high-resolution fault model for further scientific research. For example, in hours, the use of waveform modeling, earthquake slips, and seismic moment can be calculated. However, to stabilize the waveform inversions, many efforts should be made, for example, setting proper parameters such as source extent and rupture speed, which vary over a
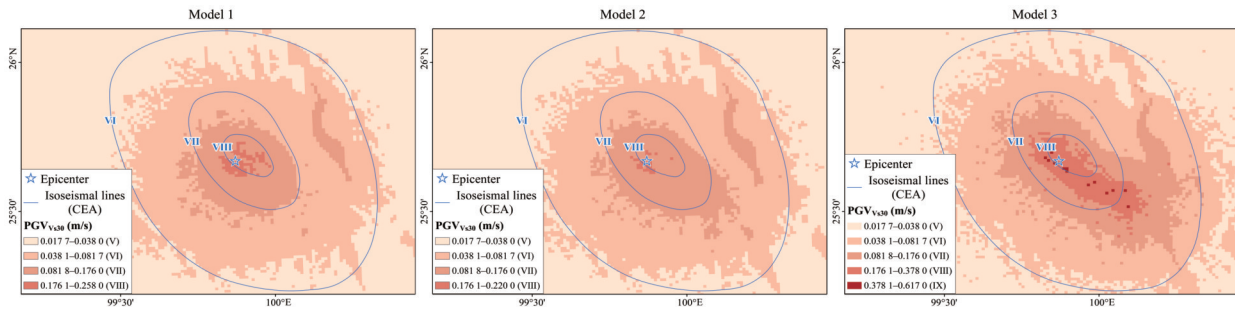
Figure 4. Estimated PGV$_{Vs30}$ of the 2021 *M*w 6.1 Yangbi Earthquake around the source region. The blue contour lines represent the contours of seismic intensities from field investigations conducted by the CEA. Three different strategies of utilizing back-projection results are employed in the three models, which contributes some variations to the estimated seismic intensity maps. The blue star indicates the epicenter of the *M*w 6.1 Yangbi Earthquake.
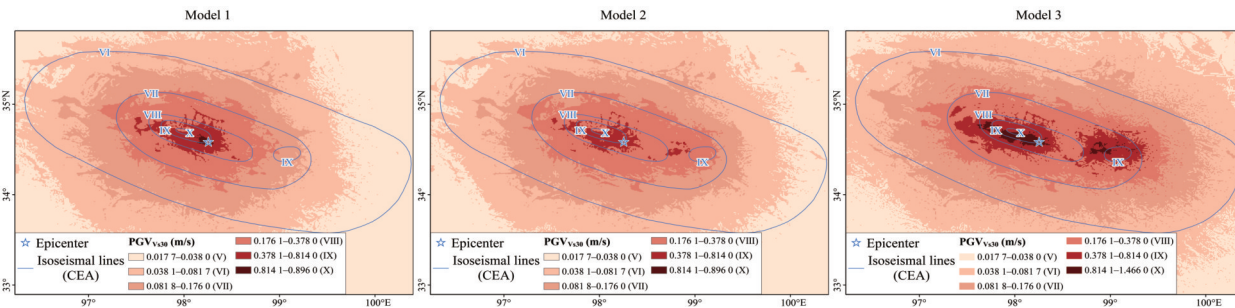

Figure 5. Shows the same information as Fig. 4 except for the 2021 *M*w 7.3 Madoi Earthquake.
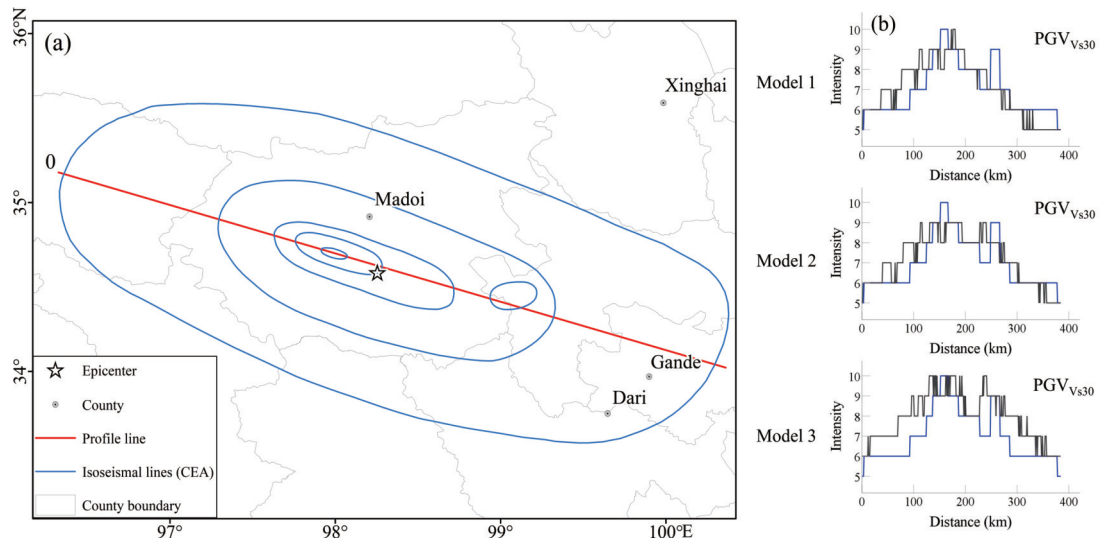

Figure 6. (a) The red line represents the profile line shown in (b), and the blue contour lines represent the contours of seismic intensities from field investigations conducted by the CEA. (b) Comparisons between calculated (black) and investigated (blue) seismic intensities along the profile line shown in (a).

large range and vary case by case. The rupture velocity of shallow earthquakes could be as fast as 5 km/s (e.g., the 2010 *M*w 6.9 Yushu and 2012 *M*w 8.6 Sumatra earthquakes), or as slow as 1 km/s (e.g., the 2006 *M*w 7.7 Java Earthquake), which cannot be resolved by regular waveform modeling that utilizes mostly tele-seismic observations. With back-projection results, we could set the fault parameters (e.g., rupture extent) precisely to, stabilize the waveform modeling and obtain an accurate slip model within a few hours after earthquakes.

5.2 Different Models

Based on our present strategies, we utilized back-projection

results to establish earthquake sources. Models 1 and 2 produced a multi-point source model, and the weighted sum of the multi-point sources contributed to the final seismic intensities.

Model 3 generated a fault plane, and the seismic intensity was calculated using the GMPEs with the shortest distance to the fault plane. Based on the application of this method to several earthquakes, including the 2008 *M*w 7.9 Wenchuan, the 2010 *M*w 6.9 Yushu, Qinghai, and the two earthquakes presented in this study, we found that Model 3 works best for large earthquakes with considerable source extents. Because of complexity of the earthquake energy radiation (e.g., frequency dependency), the relative amplitudes of the stacked energies

can't fully represent the seismic moments or radiated energies on the fault plane. Therefore, Model 3 simplified the source information by utilizing only the minimum distance from the sites to the locations of multiple sources. This simplification helps to outline the geometry of ruptured fault(s). For large earthquakes, the contour lines of the isoseismal curves were mainly controlled by the fault geometry. With accurate fault geometry, the pattern of isoseismal curves could be well constrained. For the Madoi Earthquake, our results showed a slightly curved fault, which is consistent with the surface rupture mapped by field investigations (Pan et al., 2021). The calculated intensity contour lines showed similar orientations (Fig. 6), which was also confirmed by the seismic intensity map investigated by the CEA teams.

Model 1 is more suitable for moderate earthquakes, that is, earthquakes with magnitudes <6.5, (e.g., the Mw 6.1 Yangbi, Yunan Earthquake). For such earthquakes, the source extent was approximately 20 km or less. The locations of the radiated energies were more concentrated in the epicentral area, which is more like a point source than large earthquakes with substantial source extents. In this case, given the same GMPEs, a point source assumption and finite fault model do not cause significant differences in estimating seismic intensity maps. In particular, considering that the back-projection results could not resolve the geometry of moderate earthquakes well, Model 1

mainly used the subevents that were concentrated in the epicentral area, and showed better estimates of the seismic intensity map for the Yangbi Earthquake.

5.3 Confirmation of Results with ShakeMap, DYFI, and Early Aftershock Distribution

For the Madoi Earthquake, the rupture propagated bilaterally 70 km east and west. Usually, the back-projection algorithm determines the most probable source location according to the stacked amplitudes of grid points, which may be biased due to the rupture directivity and azimuth of the seismic array. For example, the east rupture segment of the Madoi Earthquake was illustrated more poorly than the west segment because the European stations were in the forward direction of the west segment rupture.

Therefore, complementary confirmation of the rupture extent and damaged areas was needed from other resources. For example, with the advances in AI technology and its application in seismology, early aftershocks of large earthquakes can be well determined (Yang et al., 2022). Their locations can delineate the general features of the ruptured fault(s), which offers independent information about the earthquake rupture and can be used to validate the back-projected source geometry and the estimated seismic intensity map. People feel reports such as Did You Feel It? The DYFI program collects information from
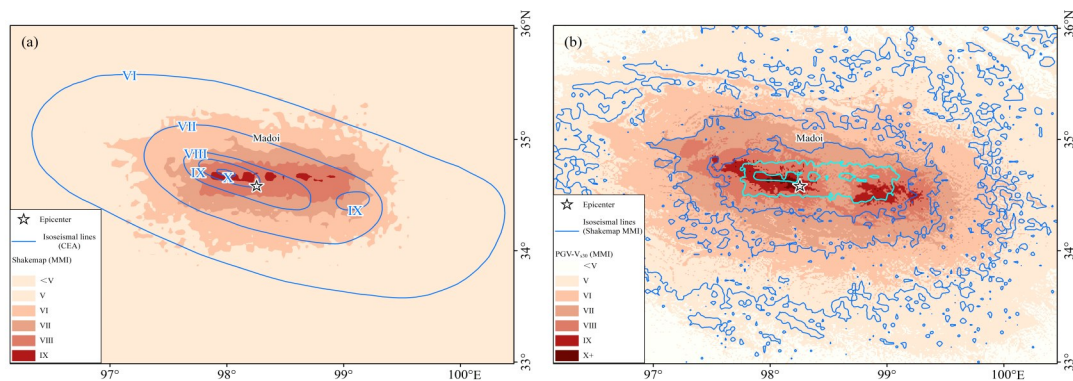

Figure 7. (a) Comparisons between the seismic intensity maps determined by the field surveys (blue lines) and the ShakeMap program (red contours) for the 2021 Madoi Earthquake. (b) Similar to (a), except the cyan and blue lines indicate the seismic contour lines determined by the ShakeMap program (USGS) and the red contours relate to our estimates.
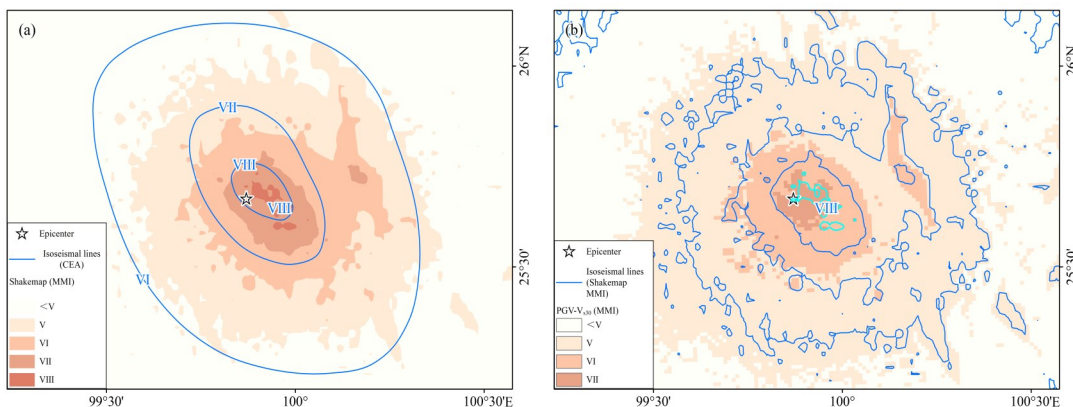

Figure 8. (a) Comparisons between the seismic intensity maps determined by the field surveys (blue lines) and the ShakeMap program (red contours) for the 2021 Yangbi Earthquake. (b) Similar to (a), except the cyan and blue lines indicate the seismic contour lines determined using the ShakeMap program (USGS) and the red contours relate to our estimates.

people who felt an earthquake and created maps that show what people experienced and the extent of damage (USGS); hence, they can offer direct verification of the seismic intensity map. Comprehensive integration of information from multiple resources would make the seismic intensity map more accurate. Comparisons among shaking map estimates by Shake-Map, USGS, CEA (Figs. 7 and 8), and this study indicate that the severely damaged areas were well outlined in our results, validating the effectiveness of this approach.

6 CONCLUSIONS

We back-projected the seismic data recorded at the European station to estimate the source processes of the 2021 *M*w 7.3 Madoi, Qinghai and the *M*w 6.1 Yangbi, Yunnan, China earthquakes. Then we summed the contributions of each subevent or estimated the shortest distances from each site to the ruptured faults, and obtained the ground motion (PGA and PGV) for each site under rock site conditions. The estimated PGVs were corrected for local site amplification using the Vs30 database (USGS).

This study validated the effectiveness of the novel approach and pushed the limit of earthquake size to as small as ~*M* 6. Therefore, it can be applied to many moderately damaging earthquakes that frequently occur in continents with severe damage. Such efforts would substantially help fast and accurate evaluation of earthquake damage, precise rescue efforts, and follow-up scientific research.

REFERENCES CITED

Atkinson, G. M., Wald, D. J., 2007. "Did You Feel It?" Intensity Data: A Surprisingly Good Measure of Earthquake Ground Motion. *Seismological Research Letters*, 78(3): 362–368 . https://doi.org/10.1785/gssrl.78.3.362

Beroza, C. G., 2013. Did You Feel It?. *Science*, 340(6130): 274–275. https://doi.org/10.1126/science.1235758

Boore, D. M., 2005. Equations for Estimating Horizontal Response Spectra and Peak Acceleration from Western North American Earthquakes: A Summary of Recent Work. *Seismological Research Letters*, 76(3): 368–369. https://doi.org/10.1785/gssrl.76.3.368

Chen, W. K., Wang, D., Si, H. J., et al., 2022. Rapid Estimation of Seismic Intensities Using a New Algorithm that Incorporates Array Technologies and Ground-Motion Prediction Equations (GMPEs). *Bulletin of the Seismological Society of America*, 112(3): 1647–1661. https://doi.org/10.1785/0120210207

Cui, H. W., Wan, Y. G., Wang, X. S., et al., 2021. Characteristic of Tectonic Stress Field in Source Region of 2018 MW 7.6 Palu Earthquake and Sulawesi Area. *Earth Science*, 46(7): 2657–2674. https://doi.org/10.3799/dqkx.2020.243 (in Chinese with English Acstract)

Dong, L. G., Shan, J., 2013. A Comprehensive Review of Earthquake-Induced Building Damage Detection with Remote Sensing Techniques. *ISPRS Journal of Photogrammetry and Remote Sensing*, 84: 85–99. https://doi.org/10.1016/j.isprsjprs.2013.06.011

Fan, X. M., van Westen, C. J., Xu, Q., et al., 2012. Analysis of Landslide Dams Induced by the 2008 Wenchuan Earthquake. *Journal of Asian Earth Sciences*, 57: 25–37. https://doi.org/10.1016/j.jseaes.2012.06.002

Farhadi, A., Pezeshk, S., 2020. A Referenced Empirical Ground-Motion Model for Arias Intensity and Cumulative Absolute Velocity Based on the NGA-East Database. *Bulletin of the Seismological Society of America*, 110(2): 508–518. https://doi.org/10.1785/0120190267

Fukushima, Y., Tanaka, T., 1990. A New Attenuation Relation for Peak Horizontal Acceleration of Strong Earthquake Ground Motion in Japan. *Bulletin-Seismological Society of America*, 80(4): 757–783.

Gamba, P., Casciati, F., 1998. GIS and Image Understanding for Near-Real-Time Earthquake Damage Assessment: Remote Sensing and GIS for Hazards. *Photogrammetric Engineering & Remote Sensing*, 64(10): 987–994

General Administration of Quality Supervision, Inspection and Quarantine. Standardization Administration, 2020. The Chinese Seismic Intensity Scale (GB/T 17742-2020). Standards Press of China, Beijing (in Chinese)

Gong, J. H., Wang, D. C., Li, Y., et al., 2010. Earthquake-Induced Geological Hazards Detection under Hierarchical Stripping Classification Framework in the Beichuan Area. *Landslides*, 7(2): 181–189. https://doi.org/10.1007/s10346-010-0201-4

Ha, G. H., Liu, J. R., Ren, Z. K., et al., 2022. The Interpretation of Seismogenic Fault of the Maduo *M*w 7.3 Earthquake, Qinghai Based on Remote Sensing Images—A Branch of the East Kunlun Fault System. *Journal of Earth Science*, 33(4): 857–868. https://doi.org/10.1007/s12583-021-1556-2

He, X. L., Xu, C., Qi, W. W., et al., 2021. Landslides Triggered by the 2020 Qiaojia *M*w 5.1 Earthquake, Yunnan, China: Distribution, Influence Factors and Tectonic Significance. *Journal of Earth Science*, 32(5): 1056–1068. https://doi.org/10.1007/s12583-021-1492-1

Krüger, F., Ohrnberger, M., 2005. Tracking the Rupture of the *M*w = 9.3 Sumatra Earthquake over 1 150 km at Teleseismic Distance. *Nature*, 435(7044): 937–939. https://doi.org/10.1038/nature03696

Lee, R., Kiremidjian, A. S., 2007. Uncertainty and Correlation for Loss Assessment of Spatially Distributed Systems. *Earthquake Spectra*, 23 (4): 753–770. https://doi.org/10.1193/1.2791001

Liu, K. S., Tsai, Y. B., Lin, P. S., 2013. A Study on Fault-Type and Site-Effect (VS30) Parameters in the Attenuation Relationships of Peak Ground Acceleration and Peak Ground Velocity in Ilan, Taiwan. *Bulletin of the Seismological Society of America*, 103(3): 1823–1845. https://doi.org/10.1785/0120120065

Matsuoka, M., Yamazaki, F., 2004. Use of Satellite SAR Intensity Imagery for Detecting Building Areas Damaged Due to Earthquakes. *Earthquake Spectra*, 20(3): 975–994 . https://doi.org/10.1193/1.1774182

Midorikawa, S., 1994. Site Effects on Strong-Motion Records Observed during the 1987 Chiba-Ken-Toho-Oki, Japan Earthquake. *Environmental Science*, 9(3): 85–90

Musson, R. M. W., 2005. Intensity Attenuation in the U. K.. *Journal of Seismology*, 9(1): 73–86. https://doi.org/10.1007/s10950-005-2979-4

Ohno, S., Ohta, T., Ikeura, T., et al., 1993. Revision of Attenuation Formula Considering the Effect of Fault Size to Evaluate Strong Motion Spectra in near Field. *Tectonophysics*, 218(1/2/3): 69–81. https://doi.

org/10.1016/0040-1951(93)90260-q

Pan, J. W., Bai, M. K., Li, C., et al., 2021. Coseismic Surface Rupture and Seismogenic Structure of the 2021-05-22 Maduo (Qinghai) Ms 7.4 Earthquake. *Acta Geologica Sinica*, 95(6): 1655–1670 (in Chinese with English Abstract)

Pathier, E., Fielding, E. J., Wright, T. J., et al., 2006. Displacement Field and Slip Distribution of the 2005 Kashmir Earthquake from SAR Imagery. *Geophysical Research Letters*, 33(20): L20310. https://doi.org/10.1029/2006gl027193

Ren, J. J., Zhang, S. M., Hou, Z. H., et al., 2007. Study of Late Quaternary Slip Rata in the Mid Segment of the Tongdian Weishan Fault. *Seismology and Geology*, 29(4): 756 – 764 (in Chinese with English Abstract)

Ren, Z. K., Zhang, Z. Q., 2019. Structural Analysis of the 1997 Mw 7.5 Manyi Earthquake and the Kinematics of the Manyi Fault, Central Tibetan Plateau. *Journal of Asian Earth Sciences*, 179: 149–164. https://doi.org/10.1016/j.jseaes.2019.05.003

Sharma, R. C., Tateishi, R., Hara, K., et al., 2017. Earthquake Damage Visualization (EDV) Technique for the Rapid Detection of Earthquake-Induced Damages Using SAR Data. *Sensors* (*Basel, Switzerland*), 17 (2): 235. https://doi.org/10.3390/s17020235

Si, H. J., Midorikawa, S., 1999. New Attenuation Relationships for Peak Ground Acceleration and Velocity Considering Effects of Fault Type and Site Condition. *Journal of Structural and Construction Engineering* (*Transactions of AIJ*), 64(523): 63–70 . https://doi.org/10.3130/aijs.64.63_2 (in Japanese)

Smith, E. M., Mooney, W. D., 2021. A Seismic Intensity Survey of the 16 April 2016 Mw 7.8 Pedernales, Ecuador, Earthquake: A Comparison with Strong-Motion Data and Teleseismic Backprojection. *Seismological Research Letters*, 92(4): 2156–2171 . https://doi.org/10.1785/0220200290

Song, C., Yao, Q., Wang, D., 2019. Magnitude of the 23 January 2018 M 7.9 Alaska Earthquake Estimated from Local Dense Seismic Records in Alaska. *Journal of Earth Science*, 30(5): 1005–1009. https://doi.org/10.1007/s12583-019-1215-z

Suga, Y., Takeuchi, S., Oguro, Y., et al., 2001. Application of ERS-2/SAR Data for the 1999 Taiwan Earthquake. *Advances in Space Research*, 28 (1): 155–163. https://doi.org/10.1016/S0273-1177(01)00334-9

Thompson, E. M., Wald, D. J., Worden, C. B., 2014. A VS30 Map for California with Geologic and Topographic Constraints. *Bulletin of the Seismological Society of America*, 104(5): 2313–2321. https://doi.org/10.1785/0120130312

USGS, 2021. M 7.3—Southern Qinghai, China. (2021-05-21). [2022-02-18]. https://earthquake.usgs.gov/earthquakes/eventpage/us7000e54r/shakemap/intensity

USGS, 2021. M 6.1—25 km NW of Dali, China. (2021-05-21). [2022-02-18]. https://earthquake.usgs.gov/earthquakes/eventpage/us7000e532/shakemap/intensity

Wald, D. J., Quitoriano, V., Heaton, T. H., et al., 1999. TriNet "ShakeMaps": Rapid Generation of Peak Ground Motion and Intensity Maps for Earthquakes in Southern California. *Earthquake Spectra*, 15 (3): 537–555. https://doi.org/10.1193/1.1586057

Wald, D. J., Quitoriano, V., Worden, C. B., et al., 2012. USGS "Did You Feel It?" Internet-Based Macroseismic Intensity Maps. *Annals of Geophysics*, 54(6): 688–707. https://doi.org/10.4401/ag-5354

Wang, D., Mori, J., 2012. The 2010 Qinghai, China, Earthquake: A Moderate Earthquake with Supershear Rupture. *Bulletin of the Seismological Society of America*, 102(1): 301–308. https://doi.org/10.1785/0120110034

Wang, D., Takeuchi, N., Kawakatsu, H., et al., 2016. Estimating High Frequency Energy Radiation of Large Earthquakes by Image Deconvolution Back-Projection. *Earth and Planetary Science Letters*, 449: 155–163. https://doi.org/10.1016/j.epsl.2016.05.051

Wang, D. C., Ni, S. D., Li, J., 2013. Research Status of Rapid Assessment on Seismic Intensity. *Progress in Geophys*, 28(4): 1772 – 1784 (in Chinese with Abstract)

Wang, W. L., Fang, L. H., Wu, J. P., et al., 2021. Aftershock Sequence Relocation of the 2021 Ms 7.4 Maduo Earthquake, Qinghai, China. *Science China Earth Sciences*, 64(8): 1371–1380 . https://doi.org/10.1007/s11430-021-9803-3

Wang, X. Q., Dou, A. X., Wang, L., et al., 2015. RS-Based Assessment of Seismic Intensity of the 2013 Lushan, Sichuan, China M_{S} 7.0 Earthquake. *Chinese Journal of Geophysics*, 58(1): 163–171 (in Chinese with Abstract)

Yang, J. W., Ye, B., Gao, Q., et al., 2021. Travel-Time Variations before and after the Yangbi Ms 6.4 Earthquake in 2021 Derived from Active-Source Seismic Data. *China Earthquake Engineering Journal*, 43(4): 767–776 (in Chinese with English Abstract)

Yang, T., Li, B. R., Fang, L. H., 2022. Relocation of the Foreshocks and Aftershocks of the 2021 Ms 6.4 Yangbi Earthquake Sequence, Yunnan, China. *Journal of Earth Science*, 33(4): 892 – 900. https://doi.org/10.1007/s12583-021-1527-7

Yao, Q., Wang, D., Fang, L. H., et al., 2019. Rapid Estimation of Magnitudes of Large Damaging Earthquakes in and around Japan Using Dense Seismic Stations in China. *Bulletin of the Seismological Society of America*, 109(6): 2545–2555 . https://doi.org/10.1785/0120190107

Yunnan Province Seismological Bureau, 2021. Intensity Map of Yangbi M 6.4 Earthquake in Yunnan Province Released. (2021-05-25). [2022-02-18]. http://www. yndzj. gov. cn/yndzj/_300559/_300651/629959/index.html

Zhang, C., Chen, W. K., Si, H. J., et al., 2021. Intensity Rapid Evaluation of Maduo M 7.4 Earthquake in Qinghai Province, 2021. *China Earthquake Engineering Journal*, 43(4): 876 – 882 (in Chinese with English Abstract)

Zhang, P. Z., Deng, Q. D., Zhang, G. M., et al., 2003. Strong Earthquake Activity and Active Blocks in Chinese Mainland. *Scientia Sinica* (*Terrae*), 33(S1): 12–20 (in Chinese with English Abstract)

Zhang, H., Ge, Z., 2010. Tracking the Rupture of the 2008 Wenchuan Earthquake by Using the Relative Back-Projection Method. *Bulletin of the Seismological Society of America*, 100(5B): 2551–2560. https://doi.org/10.1785/0120090243

Zhang, K. L., Gan, W. J., Liang, S. M., et al., 2021. The Coseismic Displacement and Slip Distribution of the 2021 May 21, Ms 6.4, Yangbi Earthquake Derived from GNSS Observations. *Chinese Journal of Geophysics*: *Chinese Edition*, 64(7): 2253–2266. https://doi.org/10.6038/10.6038/cjg2021o0524 (in Chinese with Abstract)